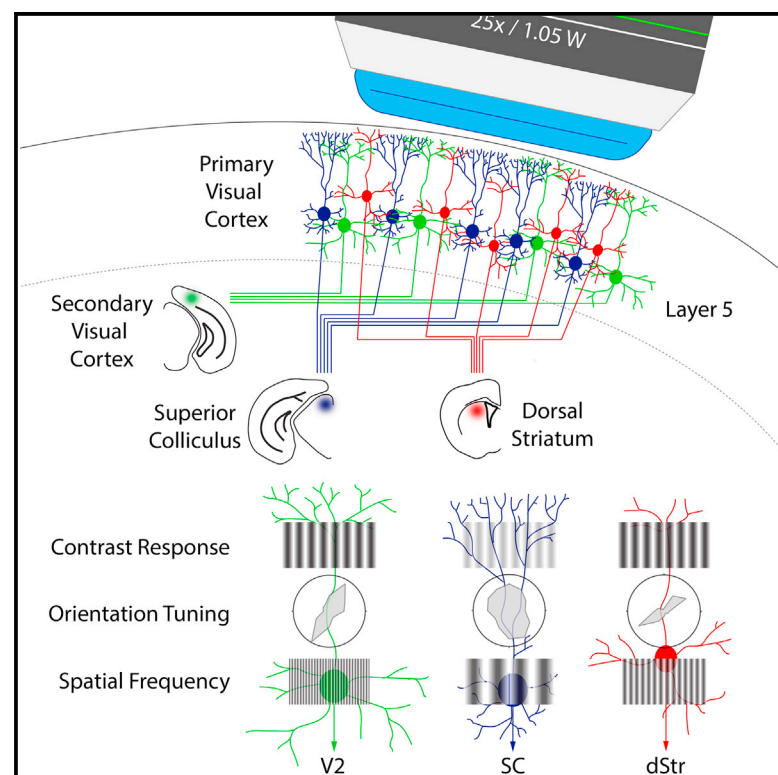# Cell Reports

Projection-Specific Visual Feature Encoding by Layer 5 Cortical Subnetworks

Graphical Abstract

Authors

Gyorgy Lur, Martin A. Vinck, Lan Tang, Jessica A. Cardin, Michael J. Higley

Correspondence

jess.cardin@yale.edu (J.A.C.),
m.higley@yale.edu (M.J.H.)

In Brief

Lur et al. demonstrate that in L5 of mouse V1, corticotectal (CT) neurons exhibit higher contrast sensitivity and broader tuning properties in comparison to corticocortical (CC) and corticostriatal (CS) neurons. Additionally, CT cell activity is broadly correlated across L5 populations, whereas CC and CS cells are more strongly correlated within their respective groups.

Highlights

- Projection targets define non-overlapping cell populations in L5 of mouse V1

- Corticotectal neurons are most broadly tuned for orientation and spatial frequency

- Corticostriatal and corticocortical neurons form correlated subnetworks in L5

CellPress

Projection-Specific Visual Feature Encoding by Layer 5 Cortical Subnetworks

Gyorgy Lur,[1,2] Martin A. Vinck,[1] Lan Tang,[1,2] Jessica A. Cardin,[1,3,*] and Michael J. Higley[1,2,3,*]
[1]Department of Neuroscience, Kavli Institute for Neuroscience
[2]Program in Cellular Neuroscience, Neurodegeneration and Repair
Yale School of Medicine, New Haven, CT 06520, USA
[3]Co-senior author
*Correspondence: jess.cardin@yale.edu (J.A.C.), m.higley@yale.edu (M.J.H.)

SUMMARY

Primary neocortical sensory areas act as central hubs, distributing afferent information to numerous cortical and subcortical structures. However, it remains unclear whether each downstream target receives a distinct version of sensory information. We used in vivo calcium imaging combined with retrograde tracing to monitor visual response properties of three distinct subpopulations of projection neurons in primary visual cortex. Although there is overlap across the groups, on average, corticotectal (CT) cells exhibit lower contrast thresholds and broader tuning for orientation and spatial frequency in comparison to corticostriatal (CS) cells, whereas corticocortical (CC) cells have intermediate properties. Noise correlational analyses support the hypothesis that CT cells integrate information across diverse layer 5 populations, whereas CS and CC cells form more selectively interconnected groups. Overall, our findings demonstrate the existence of functional subnetworks within layer 5 that may differentially route visual information to behaviorally relevant downstream targets.

INTRODUCTION

Recent evidence suggests that transmission of sensory information over distinct channels to different downstream targets is a key feature of cortical circuits (Wang and Burkhalter, 2013). Indeed, primary sensory cortex may act as a hub for routing information streams from a locally heterogeneous population of pyramidal neurons (PNs) (Glickfeld et al., 2013; Jarosiewicz et al., 2012). However, the extent to which pools of PNs extract distinct feature information from sensory inputs remains unclear. The relationships between sensory processing and functional connectivity within local and long-distance cortical networks are also poorly understood.

In the visual cortex, connection probability is elevated for neurons sharing similar feature selectivity (Ko et al., 2011; Kohn and

Smith, 2005; Okun et al., 2015). However, this relationship between connectivity and sensory tuning is not exclusive, as not all connected neurons respond to identical features (Ko et al., 2014). In addition, not all connected neurons share the same target structures (Brown and Hestrin, 2009). Along with diverse intracortical projections, V1 projects heavily from layers 2/3 and 5 to subcortical structures, including the basal ganglia and tectum (Khibnik et al., 2014; Oh et al., 2014).

Data from ex vivo preparations suggest that different populations of PNs in layer 5 (L5) may be functionally distinct. For example, corticotectal (CT) neurons projecting to the superior colliculus (SC) have thick apical trunks with prominent dendritic tuft arborizations and express high levels of hyperpolarization and cyclic nucleotide gated channels (HCNs) (Harris and Shepherd, 2015; Kasper et al., 1994). In contrast, non-CT cells, including corticostriatal (CS) and corticocortical (CC) neurons, have more modest apical dendritic tufts and exhibit little HCN expression (Shepherd, 2013; Larkman and Mason, 1990). Moreover, distinct L5 populations are differentially connected with superficial layers and with each other, suggesting the existence of distinct subnetworks within neocortical circuits (Lefort et al., 2009; Feldmeyer, 2012). Indeed, in mouse visual cortex, intragroup synaptic connectivity is highest for CS cells, contrasting with CT cells that broadly receive inputs from diverse L5 populations (Brown and Hestrin, 2009).

Previous in vivo work has shown that, in general, L5 neurons are more broadly tuned for orientation and spatial frequency than neurons in more-superficial layers (Niell and Stryker, 2008; Hoy and Niell, 2015). However, it is less clear how visual response properties vary across distinct cellular populations in L5. The striatum and SC are postulated to play important yet distinct roles in visually guided behavior (Sahibzada et al., 1986; Ragozzino et al., 2002), and the nature of the visual information directed to these areas from V1 is unclear. One possibility is that subcortical structures all receive a composite visual output, maximizing the efficacy and redundancy of visual signal transmission. Alternatively, subcortical projections may provide target-specific information content about visual features in the environment.

To address this issue, we combined retrograde fluorescent labeling with in vivo multiphoton calcium imaging to compare visual feature extraction across identified L5 PN populations. We
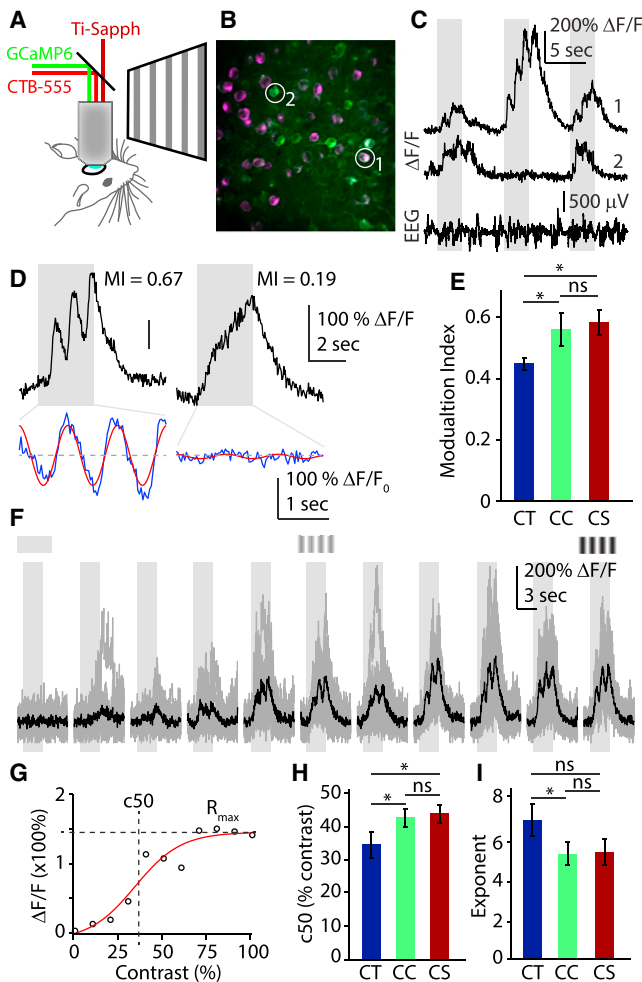
Figure 1. CT Cells Exhibit Lower Visual Detection Threshold than CC and CS Neurons

(A) Schematic of in vivo two-photon Ca^{2+} imaging of labeled L5 PN populations.

(B) Example field of view. Green somata express GCaMP6s. Magenta cells express GCaMP6s and are retrogradely labeled with red fluorescent CTB-Alexa Fluor 555.

(C) Example raw traces recorded from cells indicated in (B) and corresponding EEG signal.

(D) Example ΔF/F traces (black) and de-trended visual responses (blue) with best fit sine waves (red) to calculate modulation index (MI).

(E) Bars represent mean ± SEM MI for CT (blue), CC (green), and CS (red) cells.

(F) Example raw (gray) and average (black) ΔF/F traces recorded at varying contrast values.

(G) Hyperbolic ratio function fit (red) to contrast response (black circles). Dashed lines highlight c50 and R$_{max}$ points.

(H) Bars represent mean ± SEM c50 values of CT (blue), CC (green), and CS (red) cells.

(I) Bars represent mean ± SEM exponent values of CT (blue), CC (green), and CS (red) cells.

*$p < 0.05$; Student's t test; semi-weighted statistics (see Experimental Procedures).

find that CS, CC, and CT cells comprise largely non-overlapping populations in L5 of mouse V1. Furthermore, CT cells are more sensitive to low contrast and are more broadly tuned for orienta-

tion and spatial frequency than CS cells, whereas CC cells exhibit intermediate properties. Both CS and CC cells exhibit strong intra-group correlational structure, suggesting they form distinct subnetworks in L5, whereas CT cells show broad correlations across groups. These findings indicate that visual features may be differentially extracted by target-specific sub-networks of L5 PNs that route behaviorally relevant information to divergent downstream areas.

RESULTS

Distinct Populations of PNs in V1 L5

Previous studies have suggested that L5 comprises diverse groups of PNs that differ in their projection targets, morphology, and electrophysiological characteristics (Hattox and Nelson, 2007; Shepherd, 2013; Harris and Shepherd, 2015; Kasper et al., 1994; Larkman and Mason, 1990). To investigate the distinct functional properties of L5 PN subpopulations in V1, we combined fluorescent retrograde labeling with in vivo two-photon calcium (Ca^{2+}) imaging in lightly anesthetized mice (Figures 1A–1C, S1A, and S1B). We identified three separate groups of PNs by injecting the retrograde tracer cholera toxin B (CTB) into either the superior colliculus (SC), dorsal striatum (dStr), or contralateral medial V2 (cV2) (Figure S1C; see Experimental Procedures). Using double injections of green and red fluorescent CTB, we confirmed that labeled populations in V1 are largely non-overlapping (<2% overlap) for the three classes (Figures S1D and S1E), which also differed in their morphology and intrinsic electrophysiological characteristics (Figures S1G–S1I; Table S1). Notably, CT, CS, and CC cells showed considerable overlap in their distribution as a function of cortical depth (Figure S1F).

Visual Feature Encoding by L5 PNs

For functional imaging, we injected red fluorescent CTB into one of the three target areas and expressed GCaMP6s (Chen et al., 2013) in V1 using a viral vector. We imaged 1,525 neurons in 20 animals, of which 1,279 were deemed visually responsive (see Experimental Procedures). Of these, 950 were identified by tracer injection (342 CT cells from six animals; 306 CC neurons from nine animals; 302 CS cells from five animals). The fraction of visually responsive cells was similar in all three populations (CT: 83%; CC: 80%; CS: 83%). Each cell was imaged during presentation of one or more visual stimulus sequences, consisting of whole-field sinusoidal drifting gratings with varied contrast, orientation, and spatial frequency. Importantly, ex vivo imaging revealed no differences across cell types with regard to the relationship between spiking and calcium signal (Figures S2A–S2C).

Consistent with previous recordings of both spiking and sub-threshold activity (Hubel and Wiesel, 1962; Mechler and Ringach, 2002; Skottun et al., 1991), we observed cells whose visually evoked Ca^{2+} transients were modulated to differing degrees at the temporal frequency of the grating stimulus. We quantified this property using a modulation index (MI) (see Experimental Procedures). Cells with higher MI values are more simple-like, whereas those with lower values are more complex-like (Figure 1D). Using this metric, CT cells showed
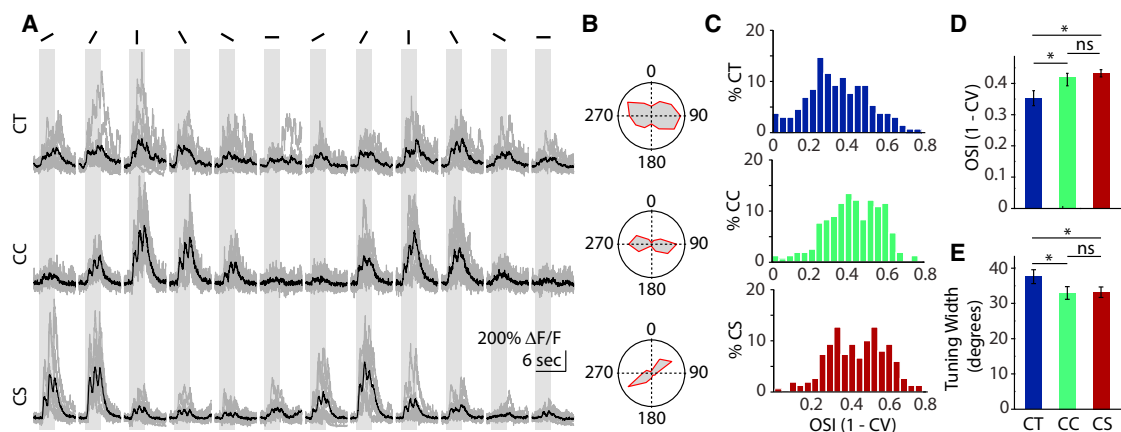
Figure 2. CT Neurons Are More Broadly Tuned for Orientation Than CC and CS Cells
(A) Example raw (gray) and average (black) traces of CT (top), CC (middle), and CS (bottom) neurons at varying orientations.
(B) Polar plots indicating the orientation tuning of the cells in (A).
(C) Distribution of OSI values for CT, CC, and CS populations.
(D) Bars represent mean ± SEM. OSI values of CT (blue), CC (green), and CS (red) cells.
(E) Bars represent mean ± SEM orientation tuning width of CT (blue), CC (green), and CS (red) cells.
*p < 0.05; Student's t test; semi-weighted statistics (see Experimental Procedures).

significantly weaker modulation (0.448 ± 0.018; n = 115; six animals) in comparison to CC (0.56 ± 0.051; n = 116; nine animals; p = 0.02; Student's t test) and CS (0.582 ± 0.037; n = 104; five animals; p = 0.0006; t test; Figures 1E and S3A). There was no difference between CC and CS cells (p = 0.36; t test). Moreover, the period of the best-fit sine wave for the data was 0.9 ± 0.2 s, in agreement with the 1-Hz temporal frequency of the stimulus. There was no significant correlation between Ca^{2+} decay and the MI (Pearson's r = −0.045; p = 0.3273; Figure S2D), suggesting that disparate Ca^{2+} buffering did not contribute to the observed MI differences. Importantly, we also found no significant differences between the decay kinetics of the Ca^{2+} signal across populations, suggesting that GCaMP6 expression is similar in the different cell groups (Figure S2E).

We then measured the sensitivity to stimulus contrast across cell populations. Only cells with a significant contrast-dependent increase in response magnitude were considered for analysis (272/438 cells; Spearman rank test r > 0 and p < 0.05; Figure 1F). For each cell, we fitted the data with a hyperbolic ratio function (Figure 1G; see Experimental Procedures; Contreras and Palmer, 2003). We calculated the c50 value, exponent, and R_{max} for the resulting curves with goodness-of-fit R^2 values > 0.4. The c50 value of CT cells (34.44% ± 3.4%; n = 70 cells; six animals) was significantly lower than that of CS cells (43.85% ± 2.3%; n = 75 cells; five animals; p = 0.0112; Student's t test) or CC cells (43.14% ± 3%; n = 108 cells; nine animals; p = 0.0285; t test; Figures 1H and S3B). Again, there was no difference between CS and CC cells (p = 0.426; t test). The exponent value was significantly higher in CT neurons (6.96 ± 0.8) than in CC cells (5.27 ± 0.57; p = 0.043; t test) but was not statistically different from CS cells (5.36 ± 0.65; p = 0.060; t test; Figures 1I and S3C). There was no significant difference between CC and CS cells (p = 0.45; t test). On average, CC cells exhibited a higher R_{max} value (0.536 ± 0.042) than CT (0.431 ± 0.027; p = 0.017; t test) or CS cells (0.411 ± 0.06; p = 0.043; t test; Figures S3D

and S3E). Together, these data indicate that, on average, CT cells are more complex-like and have a lower threshold for detecting visual stimuli compared with CS or CC cells.

We next compared the orientation tuning of the three L5 subpopulations by presenting sinusoidal drifting gratings at 100% contrast in 12 different orientations. All three groups exhibited orientation selective responses (Figures 2A, 2B, S4A, and S4B), and we therefore calculated an orientation selectivity index (OSI) (see Experimental Procedures). Across the three populations, CT cells had a significantly lower mean OSI (0.351 ± 0.021; n = 158 cells; six animals) than CC (0.42 ± 0.018; n = 193 cells; nine animals; p = 0.0071; Student's t test) or CS (0.433 ± 0.011; n = 169 cells; five animals; p = 0.0003; t test) cells, whereas the latter two were not significantly different (p = 0.2796; t test; Figures 2C and 2D). We also calculated orientation tuning width by fitting the data with a flat top von Mises function (see Experimental Procedures). Cells deemed over-fitted (extremely narrow tuning with low OSI; Figure S4C) or yielding goodness-of-fit R^2 values < 0.4 were rejected from further analysis. Tuning widths were in good agreement with OSI measures, as CT cells had significantly broader tuning (37.675 ± 1.796 degrees; n = 123 cells; six animals) than either CC (32.962 ± 1.84 degrees; n = 169 cells; nine animals; p = 0.0334; Student's t test) or CS (33.165 ± 1.4 degrees; n = 152 cells; five animals; p = 0.0263; t test) cells, whereas CC and CT cells did not differ (p = 0.4658; t test; Figure 2E). Similar results were found with an alternative measure of orientation tuning (Figure S4D). As with previous findings in non-human primates (Ringach et al., 2002), we found that the OSI is a good predictor of the tuning width for individual cells (Pearson's r = 0.4118; p < 0.001; Figure S4C). Overall, these data indicate that, as a population, CT neurons are more broadly orientation tuned than either CS or CC neurons.

In a subset of experiments, we characterized the spatial frequency preferences of identified L5 PNs (Figures 3A and S5A). Data were plotted on a log scale and fit with a Gaussian function,
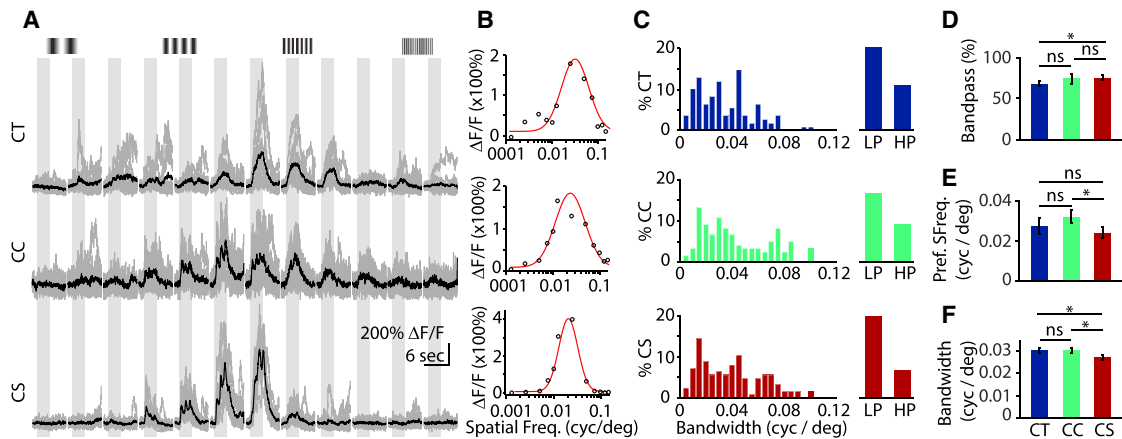
Figure 3. CC and CT Neurons Filter Spatial Frequencies at a Broader Band Than CS Cells
(A) Example raw (gray) and average (black) traces of CT (top), CC (middle), and CS (bottom) neurons at varying spatial frequencies.
(B) Gaussian curves (red) fit over spatial frequency data (black circles) from (A) on a $\log_{10}$ scale.
(C) Distributions of bandwidths and fractions of low pass (LP) and high pass (HP) for CT, CC, and CS cells.
(D) Bars represent mean ± SEM fraction of band-pass cells in CT (blue), CC (green), and CS (red) populations.
(E) Bars represent mean ± SEM preferred spatial frequency of CT (blue), CC (green), and CS (red) cells.
(F) Bars represent mean ± SEM spatial frequency bandwidth of CT (blue), CC (green), and CS (red) cells.
*$p < 0.05$; Student's t test; semi-weighted statistics (see Experimental Procedures).

allowing us to calculate the preferred spatial frequency and the bandwidth of each cell (Figures 3B and 3C). Only cells with goodness of fit $R^2 > 0.4$ were considered for further analysis. Cells were characterized as either low pass, high pass, or band pass (see Experimental Procedures; Figures S5B and S5C). For all three L5 populations, the majority of cells were band pass (Figure 3C). Furthermore, we found that CC cells exhibited higher spatial frequency preference (0.032 ± 0.003 cyc/deg; n = 176 cells; nine animals) than CS cells (0.024 ± 0.003 cyc/deg; n = 170 cells; five animals; p = 0.0293; Student's t test) but were not significantly different from CT cells (0.028 ± 0.004 cyc/deg; n = 168 cells; six animals; p = 0.165; t test). CT and CS cells did not differ (p = 0.2177; t test; Figure 3E). Notably, spatial frequency bandwidth was significantly broader for CT cells (0.303 ± 0.011 cyc/deg; p = 0.0194; t test) and CC cells (0.303 ± 0.011 cyc/deg; p = 0.0201; Student's t test) versus CS cells (0.272 ± 0.01 cyc/deg; t test), whereas CT and CC cells did not differ (p = 0.49; t test; Figure 3F). These findings suggest that both CT and CC cells are more sensitive to broadband spatial information in comparison to CS cells.

Noise Correlations Suggest Functional L5 Subnetworks
Studies in brain slices suggest that different populations of L5 PNs are selectively interconnected both within and across groups (Brown and Hestrin, 2009; Lefort et al., 2009). To assess the functional correlational structure of these circuits in vivo, we performed pairwise noise correlation analysis between individual cells (Figure S6). Higher correlation coefficients are thought to indicate a greater degree of either shared synaptic connectivity or common inputs (Cohen and Kohn, 2011; Schneidman et al., 2006). Within each field of view, we calculated the pairwise noise correlation between CTB-labeled neurons (within population) and between labeled and non-identified cells (across populations) during repeated presentation of whole-field drifting grat-

ings (Figures 4A–4E). We found that, on average, CT cells are as strongly correlated with each other ($R_{CT-CT} = 0.042 ± 0.04$) as with the non-identified neurons around them ($R_{CT-NI} = 0.04 ± 0.004$; n = 14 fields of view; six animals; p = 0.3335; paired t test). In contrast, both CC and CS cells are more strongly interconnected within their respective population than to the surrounding non-identified cells ($R_{CC-CC} = 0.046 ± 0.004$, $R_{CC-NI} = 0.024 ± 0.004$, n = 14 fields of view, nine animals, p = 0.00001, paired t test; $R_{CS-CS} = 0.04 ± 0.004$, $R_{CS-NI} = 0.025 ± 0.004$, n = 11 fields of view, five animals, p = 0.0011, paired t test; Figure 4F). These results suggest that CT cells form promiscuous local networks, whereas CC and CS cells preferentially participate in networks within their own subpopulation.

We found that activity correlation strength in all cell groups significantly decreased with increasing inter-somatic distance (Pearson's r ranging from −0.04 to −0.15; p < 0.05 in all populations; Figure 4G). Notably for CC and CS cells, the correlation within groups was significantly higher (p < 0.05 where indicated; paired t test) than across groups for short distances, indicating that group identity is important for the connectivity of local networks. We also found that pairwise correlations were related to the degree of co-tuning for orientation (Figure 4H). Again, for CC and CS cells, the correlations were higher within than across groups (p < 0.05 where indicated; paired t test). Overall, our analyses suggest that CT cells are positioned to integrate visual information across large pools of L5 neurons, whereas CC and CS are preferentially interconnected within target-specific local networks.

DISCUSSION

In this study, we characterized the functional properties of three PN subtypes in L5 of mouse V1, defined by their projection targets. We showed that CT, CS, and CC cells comprise
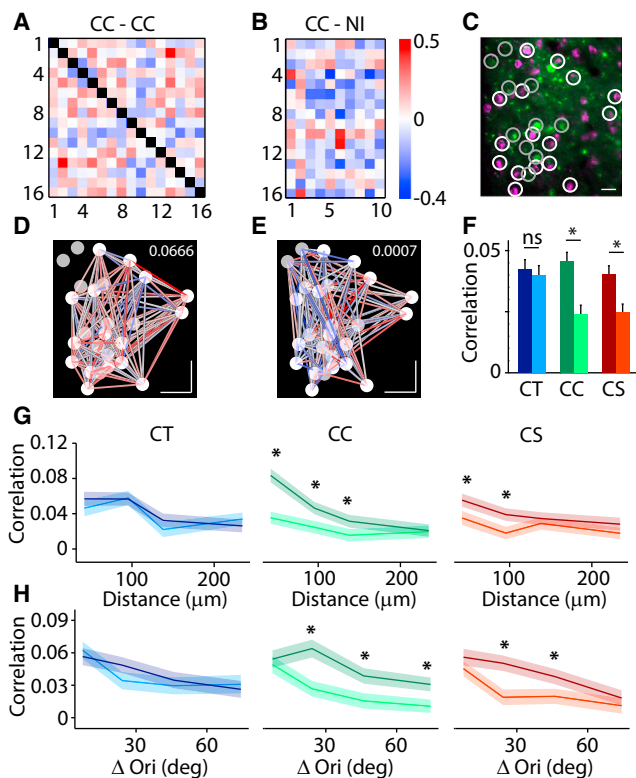
Figure 4. CC and CS Neurons Form Local Subnetworks

(A) Heatmap showing the strength of partial noise correlations between pairs of labeled CC neurons within an example field of view.

(B) Heatmap showing partial noise correlations between pairs of labeled CC and non-identified (NI) neurons in the same field of view as in (A).

(C) Two-photon fluorescent image of the field of view in (A) and (B) highlighting visually responsive CC (white circles) and NI (gray circles) neurons.

(D) Web graph showing the connections and correlation strength between CC neurons in the same field of view as in (A)–(C).

(E) Web graph showing the connections and correlation strength between CC and NI neurons in the same field of view as in (A)–(D).

(F) Bars representing mean ± SEM correlation strength between CT-CT (dark blue), CT-NI (light blue), CC-CC (dark green), CC-NI (light green), CS-CS (dark red), and CS-NI (light red) cell pairs. *p < 0.05; paired t test.

(G) Change in correlation strength with distance between CT-CT (dark blue), CT-NI (light blue), CC-CC (dark green), CC-NI (light green), CS-CS (dark red), and CS-NI (light red) cell pairs. *p < 0.05; paired t test.

(H) Change in correlation strength related to the degree of co-tuning for orientation between CT-CT (dark blue), CT-NI (light blue), CC-CC (dark green), CC-NI (light green), CS-CS (dark red), and CS-NI (light red) cell pairs. *p < 0.05; paired t test.

non-overlapping populations that display differences in contrast sensitivity, orientation tuning, and spatial frequency selectivity. In general, CT cells exhibit the highest contrast sensitivity and broadest tuning for orientation and spatial frequency, similar to a previous electrophysiological study of putative CT neurons (Mangini and Pearlman, 1980). Conversely, CS cells are more narrowly tuned for visual inputs, whereas CC cells exhibit intermediate properties. Moreover, analysis of noise correlations suggests that CT cells are widely connected to other L5 PNs, whereas CC and CS cells form more-circumscribed networks within their own groups. These

findings shed important light on the functional diversity of information processing by a cortical output layer and indicate that information streams routed to distinct downstream targets are functionally heterogeneous.

One caveat regarding our findings is that Ca^{2+} signaling may not accurately reflect underlying spike activity across different cell groups, potentially due to variations in GCaMP6 expression or nonlinearity of the indicator. However, using ex vivo imaging, we found no differences between spiking and calcium signaling for the three groups. Moreover, we found that the Ca^{2+} decay kinetics in vivo do not differ between the CT, CS, and CC cells (see Figure S2), suggesting that all cells express similar amounts of GCaMP6 (Higley and Sabatini, 2008). Finally, previous reports have suggested visually evoked firing rates for L5 PNs of less than 5 Hz (Hoy and Niell, 2015; Vinck et al., 2015), well within the linear regime for GCaMP6 signaling (Chen et al., 2013; Podor et al., 2015). Thus, we do not think it likely that variation in spike-Ca^{2+} coupling explains the observed differences in visual tuning across populations of L5 PNs.

Previous work in brain slices has demonstrated the morphological, molecular, and electrophysiological heterogeneity of L5 PNs (Hattox and Nelson, 2007; Shepherd, 2013; Larkman and Mason, 1990; Harris and Shepherd, 2015; Kasper et al., 1994). Two major cell types have been described: thin tufted cells (also referred to as type B or intratelencephalic) and thick tufted cells (also called type A or pyramidal tract). Type B cells, likely corresponding to our CC and CS cells, are thought to be located primarily in L5A and are characterized by wider action potentials, adapting firing properties, and the expression of the transcription factor SATB2 (Shepherd, 2013). Conversely, type A neurons, likely corresponding to our CT cells, are thought to be located in L5B and exhibit narrower action potentials, bursting firing patterns, and expression of CTIP2 and FEZF2 (Hattox and Nelson, 2007; Kasper et al., 1994). Notably, in the auditory cortex of the rat, intrinsic-bursting L5 PNs have broader tuning properties than regular spiking cells (Sun et al., 2013).

Work from both in vivo and ex vivo preparations has suggested the existence of synaptically coupled subnetworks within cortical microcircuits (Brown and Hestrin, 2009; Lefort et al., 2009). For example, cells that share similar visual tuning properties exhibit higher monosynaptic connection probability (Ko et al., 2011; Kohn and Smith, 2005). In addition, paired recordings of L5 PNs in V1 indicate high interconnectivity between CS cells, whereas CT cells are broadly connected with multiple L5 populations (Brown and Hestrin, 2009). Here, we analyzed noise correlations, which have been used to assess functional (though not necessarily anatomical) connectivity between neurons in vivo (Cohen and Kohn, 2011; Hofer et al., 2011; Kohn and Smith, 2005; Ecker et al., 2010; Smith and Kohn, 2008). Our results expand these previous findings to show that both CC and CS cells exhibit strong within-group correlations, suggesting preferential connectivity among like-projecting neurons. In contrast, CT cells appear to be broadly connected both within and between groups. This divergent connectivity of CT cells is further supported by their lower MI, suggesting that CT cells are more complex-like. Complex cells

are hypothesized to arise from the summed input from up-stream simple cells (Martinez and Alonso, 2003; Hubel and Wiesel, 1962), suggesting that CT cells function generally as in-tegrators. Finally, in agreement with previous findings (Hofer et al., 2011; Ko et al., 2011; Smith and Kohn, 2008), we show that functional connectivity of all groups is significantly corre-lated both with similarity of orientation tuning as well as inter-somatic distance. Again, for CC and CS cells, there is greater correlation within versus across group. Thus, our results indi-cate that projection specificity is a key additional factor in determining functional circuit interactions.

These findings indicate that subpopulations of L5 cells relay varied information about visual stimuli to different downstream targets. This conclusion is supported by recent evidence that cells in V1 that project to different ipsilateral higher-order visual areas also convey distinct spatial and temporal information (Glickfeld et al., 2013; Jarosiewicz et al., 2012; El-Shamayleh et al., 2013; Movshon and Newsome, 1996; Andermann et al., 2011). In addition, a recent study found that different genetically defined L5 PNs exhibit tuning differences similar to those seen in our work (Kim et al., 2015). Ultimately, this organization may pro-vide information necessary for appropriate processing by the target structures. For example, the SC is thought to play a prom-inent role in orienting behaviors, where fine information about spatiotemporal stimulus properties may be unnecessary (Sahib-zada et al., 1986; Dean et al., 1986). This is consistent with the high contrast sensitivity and broad tuning properties of CT cells, which may function more like "detectors." In contrast, the stria-tum plays a crucial role in motor planning and reward-based learning (Graybiel and Grafton, 2015). Furthermore, higher-order visual areas (e.g., V2) may play key roles in decision making about visually guided behaviors (Lee et al., 2002; Prusky and Douglas, 2004; Marshel et al., 2011). Therefore, cells projecting to these areas may require higher selectivity for visual features, functioning more like "discriminators." Future studies are needed to investigate the behavioral contributions of these heterogeneous L5 populations.

Lastly, we note that our approach to the statistical analysis of population data was based on the inherent nested design of the study. Analyses based on individual cells (rather than animals) face an increased false positive rate for detecting significant differences (Galbraith et al., 2010; Cochran, 1937). To address this issue, we used a statistical approach that compares means across animals (DerSimonian and Laird, 1986; Chung et al., 2013; Experimental Procedures), with individual means weighted by the variance within and across groups. This method is commonly used in random-effects meta-analyses and re-duces the false-positive rate while maintaining statistical power within acceptable limits (Aarts et al., 2014). This is an especially important analytical tool for multiphoton datasets that typically include many tens or hundreds of cells per mouse but do not involve large numbers of animals.

In conclusion, our findings indicate that, despite physical co-mingling of cell bodies, subpopulations of V1 neurons form specific functionally interconnected networks in L5 that are capable of extracting varied feature information about the vi-sual world and relaying this information to different downstream targets.

EXPERIMENTAL PROCEDURES

Animals

Adolescent (6- to 8-week-old) wild-type C57/bl6 mice (Charles River Labora-tories) were used in accordance with the Yale Institutional Animal Care and Use Committee and federal guidelines.

In Vivo Imaging

GCaMP6s was expressed in V1 using an adenoassociated virus vector (AAV2-*hSynapsin1*-GCaMP6s, serotype 5; University of Pennsylvania Vec-tor Core). Projection-specific subtypes of L5 PNs were labeled using CTB-Alexa Fluor 555 injected into the SC, dStr, or cV2. Imaging was per-formed 25–30 days after injection under light isoflurane anesthesia through an acutely implanted glass cranial window. Imaging was performed using a resonant scanner-based two-photon microscope (MOM; Sutter Instru-ments) coupled to a Ti:sapphire laser (MaiTai DeepSee; Spectra Physics) tuned to 940 nm for GCaMP6 and 1,000 nm for CTB-Alexa Fluor 555. Im-ages were acquired using ScanImage 4.2 (Vidrio Technologies) at ∼30 Hz from a depth of ∼450–600 μm relative to the brain surface. Visual stimuli consisted of full-screen sinusoidal drifting gratings with a temporal fre-quency of 1 Hz and with varied contrast, orientation, and spatial frequency. For all experiments, visual stimuli were 3 s in duration and separated by an inter-stimulus interval of 5 s.

Data Analysis

Analysis was performed using custom-written routines in MATLAB (The Math-works) and IgorPro (Wavemetrics). Regions of interest (ROIs) corresponding to single cells were selected as previously described (Chen et al., 2013). Ca^{2+} signals in response to visual stimuli were averaged and expressed as $\Delta F/F$. A cell was classified as visually responsive if the Ca^{2+} signals during stimulus presentation were statistically different from the signals during five blank periods ($p < 0.05$; ANOVA test) and larger than 10% $\Delta F/F$.

The MI for each individual cell was determined by fitting data with a sine function and normalizing the peak-to-trough amplitude by the mean total Ca^{2+} response. Contrast response curves were fit by a hyperbolic ratio func-tion (Contreras and Palmer, 2003). The OSI was calculated as $1 -$ circular vari-ance (Ringach et al., 2002). Orientation tuning bandwidth was measured as the half width at $1/\sqrt{2}$ of a flat-top von Mises function fit to the data. For spatial frequency tuning, data were plotted on a log10-frequency scale and fit with a Gaussian function. Cells were classified as low pass or high pass if the low or high end of the tuning curve, respectively, failed to cross the half maximum point. For all analyses that required curve fitting, cells were only included if the goodness of fit yielded a $R^2 > 0.4$. Noise correlations were calculated as the partial correlation coefficient between pairs of cells.

Statistical Analysis

For most analyses, we developed a method of using semi-weighted estimators to compare individual animals, rather than cells (Chung et al., 2013; DerSimonian and Laird, 1986). This approach minimizes false positives while maintaining statistical power (Aarts et al., 2014). We used this semi-weighted estimator to calculate the statistical significance of the difference between cell populations using a standard Student's t test. The only exception to this was the noise correlation analysis in Figure 4, where we used the weighted esti-mator to reflect the pairwise nature of the comparisons.

SUPPLEMENTAL INFORMATION

Supplemental Information includes Supplemental Experimental Procedures, six figures, and one table and can be found with this article online at http://dx.doi.org/10.1016/j.celrep.2016.02.050.

AUTHOR CONTRIBUTIONS

G.L., J.A.C., and M.J.H. designed and G.L. and L.T. performed the experi-ments. G.L., M.A.V., and L.T. analyzed the data. G.L., J.A.C., and M.J.H. wrote the paper.

REFERENCES

Aarts, E., Verhage, M., Veenvliet, J.V., Dolan, C.V., and van der Sluis, S. (2014). A solution to dependency: using multilevel analysis to accommodate nested data. Nat. Neurosci. 17, 491–496.

Andermann, M.L., Kerlin, A.M., Roumis, D.K., Glickfeld, L.L., and Reid, R.C. (2011). Functional specialization of mouse higher visual cortical areas. Neuron 72, 1025–1039.

Brown, S.P., and Hestrin, S. (2009). Intracortical circuits of pyramidal neurons reflect their long-range axonal targets. Nature 457, 1133–1136.

Chen, T.W., Wardill, T.J., Sun, Y., Pulver, S.R., Renninger, S.L., Baohan, A., Schreiter, E.R., Kerr, R.A., Orger, M.B., Jayaraman, V., et al. (2013). Ultrasensitive fluorescent proteins for imaging neuronal activity. Nature 499, 295–300.

Chung, Y., Rabe-Hesketh, S., and Choi, I.H. (2013). Avoiding zero between-study variance estimates in random-effects meta-analysis. Stat. Med. 32, 4071–4089.

Cochran, W.G. (1937). Problems arising in the analysis of a series of similar experiments. Supplement to the Journal of the Royal Statistical Society 4, 102–118.

Cohen, M.R., and Kohn, A. (2011). Measuring and interpreting neuronal correlations. Nat. Neurosci. 14, 811–819.

Contreras, D., and Palmer, L. (2003). Response to contrast of electrophysiologically defined cell classes in primary visual cortex. J. Neurosci. 23, 6936–6945.

Dean, P., Redgrave, P., Sahibzada, N., and Tsuji, K. (1986). Head and body movements produced by electrical stimulation of superior colliculus in rats: effects of interruption of crossed tectoreticulospinal pathway. Neuroscience 19, 367–380.

DerSimonian, R., and Laird, N. (1986). Meta-analysis in clinical trials. Control. Clin. Trials 7, 177–188.

Ecker, A.S., Berens, P., Keliris, G.A., Bethge, M., Logothetis, N.K., and Tolias, A.S. (2010). Decorrelated neuronal firing in cortical microcircuits. Science 327, 584–587.

El-Shamayleh, Y., Kumbhani, R.D., Dhruv, N.T., and Movshon, J.A. (2013). Visual response properties of V1 neurons projecting to V2 in macaque. J. Neurosci. 33, 16594–16605.

Feldmeyer, D. (2012). Excitatory neuronal connectivity in the barrel cortex. Front. Neuroanat. 6, 24.

Galbraith, S., Daniel, J.A., and Vissel, B. (2010). A study of clustered data and approaches to its analysis. J. Neurosci. 30, 10601–10608.

Glickfeld, L.L., Andermann, M.L., Bonin, V., and Reid, R.C. (2013). Corticocortical projections in mouse visual cortex are functionally target specific. Nat. Neurosci. 16, 219–226.

Graybiel, A.M., and Grafton, S.T. (2015). The striatum: where skills and habits meet. Cold Spring Harb. Perspect. Biol. 7, a021691.

Harris, K.D., and Shepherd, G.M. (2015). The neocortical circuit: themes and variations. Nat. Neurosci. 18, 170–181.

Hattox, A.M., and Nelson, S.B. (2007). Layer V neurons in mouse cortex projecting to different targets have distinct physiological properties. J. Neurophysiol. 98, 3330–3340.

Higley, M.J., and Sabatini, B.L. (2008). Calcium signaling in dendrites and spines: practical and functional considerations. Neuron 59, 902–913.

Hofer, S.B., Ko, H., Pichler, B., Vogelstein, J., Ros, H., Zeng, H., Lein, E., Lesica, N.A., and Mrsic-Flogel, T.D. (2011). Differential connectivity and response dynamics of excitatory and inhibitory neurons in visual cortex. Nat. Neurosci. 14, 1045–1052.

Hoy, J.L., and Niell, C.M. (2015). Layer-specific refinement of visual cortex function after eye opening in the awake mouse. J. Neurosci. 35, 3370–3383.

Hubel, D.H., and Wiesel, T.N. (1962). Receptive fields, binocular interaction and functional architecture in the cat's visual cortex. J. Physiol. 160, 106–154.

Jarosiewicz, B., Schummers, J., Malik, W.Q., Brown, E.N., and Sur, M. (2012). Functional biases in visual cortex neurons with identified projections to higher cortical targets. Curr. Biol. 22, 269–277.

Kasper, E.M., Larkman, A.U., Lübke, J., and Blakemore, C. (1994). Pyramidal neurons in layer 5 of the rat visual cortex. I. Correlation among cell morphology, intrinsic electrophysiological properties, and axon targets. J. Comp. Neurol. 339, 459–474.

Khibnik, L.A., Tritsch, N.X., and Sabatini, B.L. (2014). A direct projection from mouse primary visual cortex to dorsomedial striatum. PLoS ONE 9, e104501.

Kim, E.J., Juavinett, A.L., Kyubwa, E.M., Jacobs, M.W., and Callaway, E.M. (2015). Three Types of Cortical Layer 5 Neurons That Differ in Brain-wide Connectivity and Function. Neuron 88, 1253–1267.

Ko, H., Hofer, S.B., Pichler, B., Buchanan, K.A., Sjöström, P.J., and Mrsic-Flogel, T.D. (2011). Functional specificity of local synaptic connections in neocortical networks. Nature 473, 87–91.

Ko, H., Mrsic-Flogel, T.D., and Hofer, S.B. (2014). Emergence of feature-specific connectivity in cortical microcircuits in the absence of visual experience. J. Neurosci. 34, 9812–9816.

Kohn, A., and Smith, M.A. (2005). Stimulus dependence of neuronal correlation in primary visual cortex of the macaque. J. Neurosci. 25, 3661–3673.

Larkman, A., and Mason, A. (1990). Correlations between morphology and electrophysiology of pyramidal neurons in slices of rat visual cortex. I. Establishment of cell classes. J. Neurosci. 10, 1407–1414.

Lee, T.S., Yang, C.F., Romero, R.D., and Mumford, D. (2002). Neural activity in early visual cortex reflects behavioral experience and higher-order perceptual saliency. Nat. Neurosci. 5, 589–597.

Lefort, S., Tomm, C., Floyd Sarria, J.C., and Petersen, C.C. (2009). The excitatory neuronal network of the C2 barrel column in mouse primary somatosensory cortex. Neuron 61, 301–316.

Mangini, N.J., and Pearlman, A.L. (1980). Laminar distribution of receptive field properties in the primary visual cortex of the mouse. J. Comp. Neurol. 193, 203–222.

Marshel, J.H., Garrett, M.E., Nauhaus, I., and Callaway, E.M. (2011). Functional specialization of seven mouse visual cortical areas. Neuron 72, 1040–1054.

Martinez, L.M., and Alonso, J.M. (2003). Complex receptive fields in primary visual cortex. Neuroscientist 9, 317–331.

Mechler, F., and Ringach, D.L. (2002). On the classification of simple and complex cells. Vision Res. 42, 1017–1033.

Movshon, J.A., and Newsome, W.T. (1996). Visual response properties of striate cortical neurons projecting to area MT in macaque monkeys. J. Neurosci. 16, 7733–7741.

Niell, C.M., and Stryker, M.P. (2008). Highly selective receptive fields in mouse visual cortex. J. Neurosci. 28, 7520–7536.

Oh, S.W., Harris, J.A., Ng, L., Winslow, B., Cain, N., Mihalas, S., Wang, Q., Lau, C., Kuan, L., Henry, A.M., et al. (2014). A mesoscale connectome of the mouse brain. Nature 508, 207–214.

Okun, M., Steinmetz, N.A., Cossell, L., Iacaruso, M.F., Ko, H., Barthó, P., Moore, T., Hofer, S.B., Mrsic-Flogel, T.D., Carandini, M., and Harris, K.D. (2015). Diverse coupling of neurons to populations in sensory cortex. Nature *521*, 511–515.

Podor, B., Hu, Y.L., Ohkura, M., Nakai, J., Croll, R., and Fine, A. (2015). Comparison of genetically encoded calcium indicators for monitoring action potentials in mammalian brain by two-photon excitation fluorescence microscopy. Neurophotonics *2*, 021014.

Prusky, G.T., and Douglas, R.M. (2004). Characterization of mouse cortical spatial vision. Vision Res. *44*, 3411–3418.

Ragozzino, M.E., Ragozzino, K.E., Mizumori, S.J., and Kesner, R.P. (2002). Role of the dorsomedial striatum in behavioral flexibility for response and visual cue discrimination learning. Behav. Neurosci. *116*, 105–115.

Ringach, D.L., Shapley, R.M., and Hawken, M.J. (2002). Orientation selectivity in macaque V1: diversity and laminar dependence. J. Neurosci. *22*, 5639–5651.

Sahibzada, N., Dean, P., and Redgrave, P. (1986). Movements resembling orientation or avoidance elicited by electrical stimulation of the superior colliculus in rats. J. Neurosci. *6*, 723–733.

Schneidman, E., Berry, M.J., 2nd, Segev, R., and Bialek, W. (2006). Weak pairwise correlations imply strongly correlated network states in a neural population. Nature *440*, 1007–1012.

Shepherd, G.M. (2013). Corticostriatal connectivity and its role in disease. Nat. Rev. Neurosci. *14*, 278–291.

Skottun, B.C., De Valois, R.L., Grosof, D.H., Movshon, J.A., Albrecht, D.G., and Bonds, A.B. (1991). Classifying simple and complex cells on the basis of response modulation. Vision Res. *31*, 1079–1086.

Smith, M.A., and Kohn, A. (2008). Spatial and temporal scales of neuronal correlation in primary visual cortex. J. Neurosci. *28*, 12591–12603.

Sun, Y.J., Kim, Y.J., Ibrahim, L.A., Tao, H.W., and Zhang, L.I. (2013). Synaptic mechanisms underlying functional dichotomy between intrinsic-bursting and regular-spiking neurons in auditory cortical layer 5. J. Neurosci. *33*, 5326–5339.

Vinck, M., Batista-Brito, R., Knoblich, U., and Cardin, J.A. (2015). Arousal and locomotion make distinct contributions to cortical activity patterns and visual encoding. Neuron *86*, 740–754.

Wang, Q., and Burkhalter, A. (2013). Stream-related preferences of inputs to the superior colliculus from areas of dorsal and ventral streams of mouse visual cortex. J. Neurosci. *33*, 1696–1705.

Supplemental Information

Projection-Specific Visual Feature Encoding

by Layer 5 Cortical Subnetworks

Gyorgy Lur, Martin A. Vinck, Lan Tang, Jessica A. Cardin, and Michael J. Higley
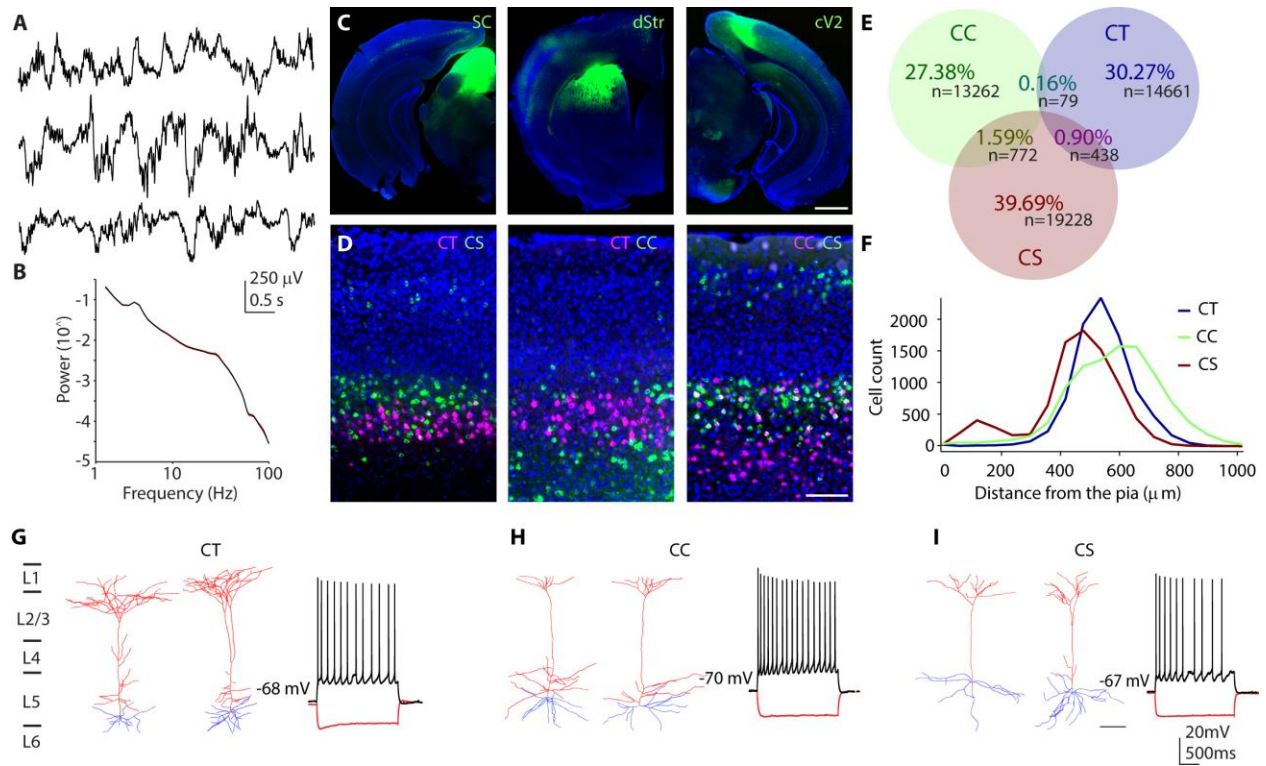
Figure S1. Anatomy and firing patterns of L5 projection neuron populations in V1, related to Figure 1.
(A) Example EEG traces from 3 different animals measured under light isoflurane anesthesia during *in vivo* Ca^{2+} imaging experiments.
(B) Mean ± SEM (black line and red shaded area) power spectrum from 51 recording sessions.
(C) Wide field fluorescent images of CTB injections sites (green) over-laid with DAPI (blue) staining. Scale bar represents 100 μm.
(D) Cell bodies of L5 PN populations labeled after dual injection of retrograde tracers into different target structures. Scale bar is 1000 μm.
(E) Venn diagram showing the degree of overlap between L5 PN populations (3 mice for each condition).
(F) Laminar distribution of CTB-labeled somata in V1.
(G) Example reconstructions of CT neurons. Basal dendrites in blue, apical dendritic arbor in red. Traces show typical responses to depolarizing (black) and hyperpolarizing (red) current injections.
(H) Example reconstructions of CC neurons. Basal dendrites in blue, apical dendritic arbor in red. Traces show typical responses to depolarizing (black) and hyperpolarizing (red) current injections.
(I) Example reconstructions of CS neurons. Basal dendrites in blue, apical dendritic arbor in red. Scale bar is 100 μm, applies to (G) and (H). Traces show typical responses to depolarizing (black) and hyperpolarizing (red) current injections.

2

	Projection Target			
	CT	CC	CS	ANOVA P
Resting Vm (mV)	-69.2 ± 1.44	-71.59 ± 2.71	-65.90 ± 2.81	0.26
Sag Ratio	0.192 ± 0.022	0.088 ± 0.017	0.108 ± 0.016	0.00044***
Time constant (ms)	160.29 ± 14.87	189.19 ± 16.17	198.56 ± 13.19	0.18
Input resistance (MOhm)	151.94 ± 16.41	180.27 ± 17.43	171.33 ± 12.53	0.43
AP Amplitude (mV)	60.18 ± 2.08	57.04 ± 1.51	57.38 ± 1.55	0.38
AP Threshold (mV)	-49.9 ± 1.07	-50.80 ± 0.97	-49.88 ± 0.89	0.99
AP Half-width (ms)	0.39 ± 0.28	0.50 ± 0.3	0.47 ± 0.26	0.014*

Table S1. Intrinsic membrane properties of L5 projection neurons in V1, related to Figure 1.
CT: n=18 cells, 3 animals, CC: 18 cells, 4 animals, CS: 19 cells, 5 animals
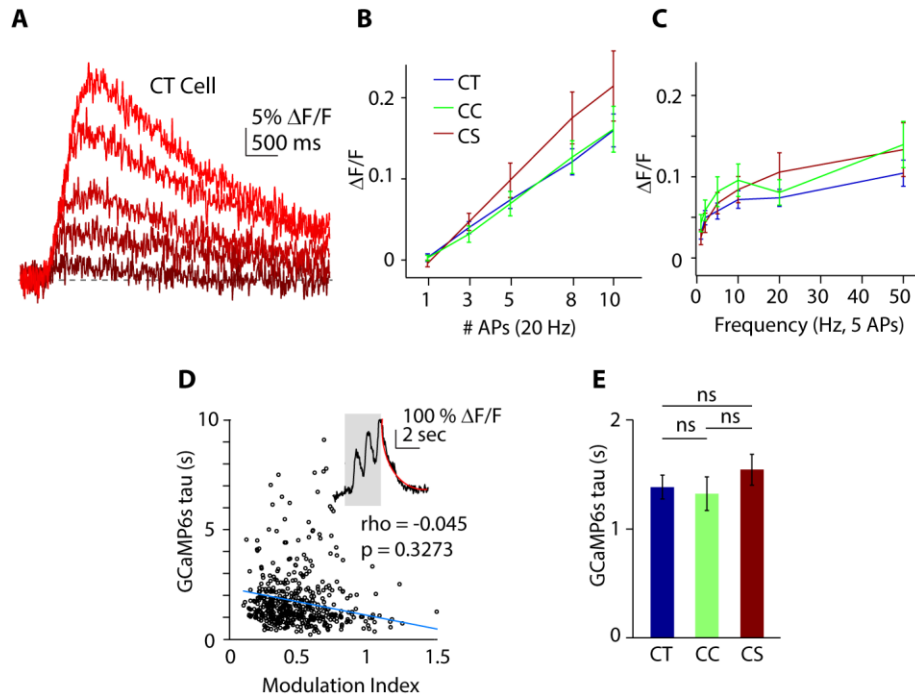Statistics: one-way ANOVA, p-value indicated in last column of the table.

Figure S2. GCaMP6s florescence change in relation to action potential firing is not cell type dependent, related to Figure 1.

(A) Example traces showing GCaMP6s fluorescence responses of an identified CT neuron to increasing number of action potentials (1-10, increasing color intensity) *in vitro*.

(B) Average fluorescence responses of identified CT (blue), CC (green), and CS (red) neurons to increasing number of action potentials (1-10). There was no difference between the cell types

(C) Average fluorescence responses of identified CT (blue), CC (green), and CS (red) neurons to 5 action potentials delivered at increasing frequencies (1-50 Hz). There was no difference between the cell types

(D) Modulation index plotted against the decay constant (tau) of GCaMP6s (n=328 cells in 20 animals) *in vivo*. Insert shows an example visually evoked calcium signal and the exponential fit to the decay phase used to calculate tau (red).

(E) Bars represent mean ± SEM of the decay constant (tau) of GCaMP6s, calculated from an exponential fit of the Ca^{2+} transients following the termination of the visual stimulus *in vivo*. CT (blue, n=117 cells, 6 animals) CC (green, n=122, 9 animals,) and CS (red, n=90cells, 5 animals) cells.
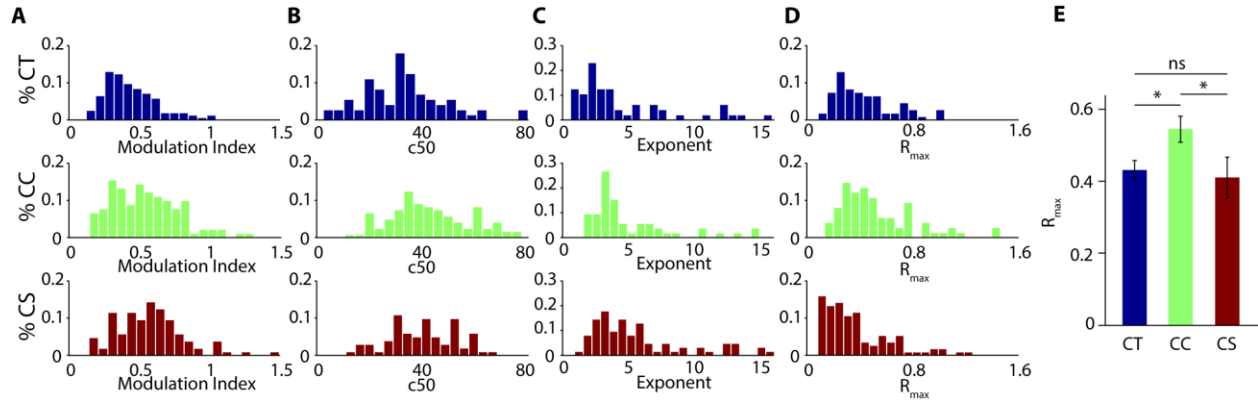
*: $p<0.05$, Student's t-test.

Figure S3. Distribution histograms showing Modulation Index, contrast response c50, exponent and R_{max} values *in vivo*, related to Figure 1.
(A) Distribution of Modulation Index values of CT (blue), CC (green) and CS (red) cells.
(B) Distribution of c50 values of CT (blue), CC (green) and CS (red) cells.
(C) Distribution of exponent values of CT (blue), CC (green) and CS (red) cells.
(D) Distribution of R_{max} values of CT (blue), CC (green) and CS (red) cells.
(E) Bars represent mean ± SEM of R_{max} of the hyperbolic ratio function fitted over contrast responses of CT (blue, n=70 cells, 6 animals) CC (green, n=108, 9 animals,) and CS (red, n=75 cells, 5 animals) cells.
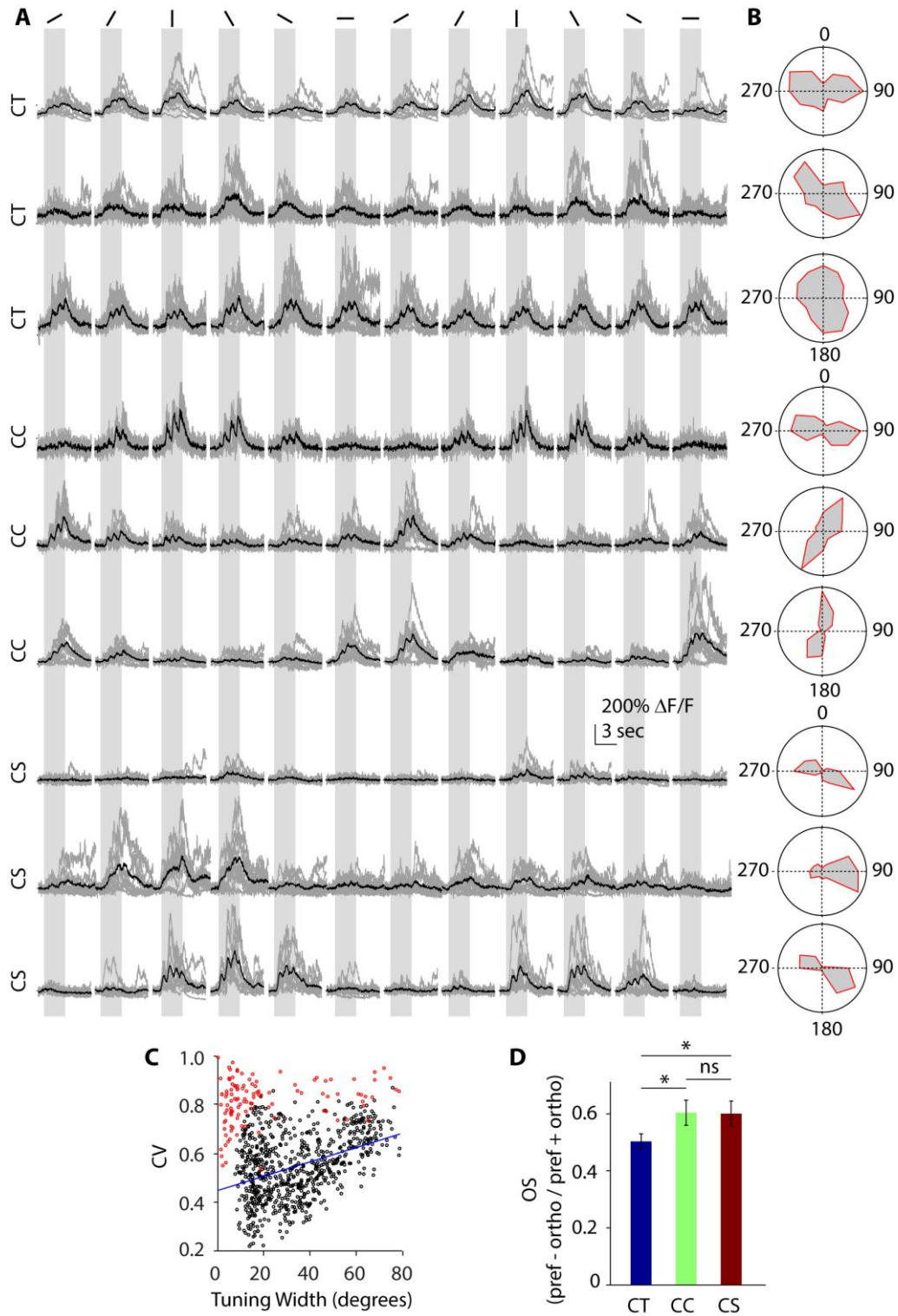*: p<0.05, Student's t-test.

Figure S4. Examples and extended analysis of orientation tuning, related to Figure 2.
(A) Example raw (gray) and average (black) traces of a CT (top three), CC (middle three) and CS (bottom three) neurons at varying orientations.
(B) Polar plots indicating the orientation tuning of the cells in (A).

(C) Orientation tuning width plotted against the circular variance of each cell. Red circles represent cells rejected from further analysis for displaying extremely narrow tuning width with high circular variance values (likely over fits, top left cluster) or for having a poor (R^2 <0.4) goodness-of-fit for the von Mises function. Blue line represents the linear fit to the data.

(D) Bars represent mean ± SEM of orientation selectivity calculated as the depth of modulation of CT (blue, n=158 cells, 6 animals), CC (green, n=193 cells, 9 animals), and CS (red, n=169 cells, 5 animals) cells.

*: p<0.05, t-test.
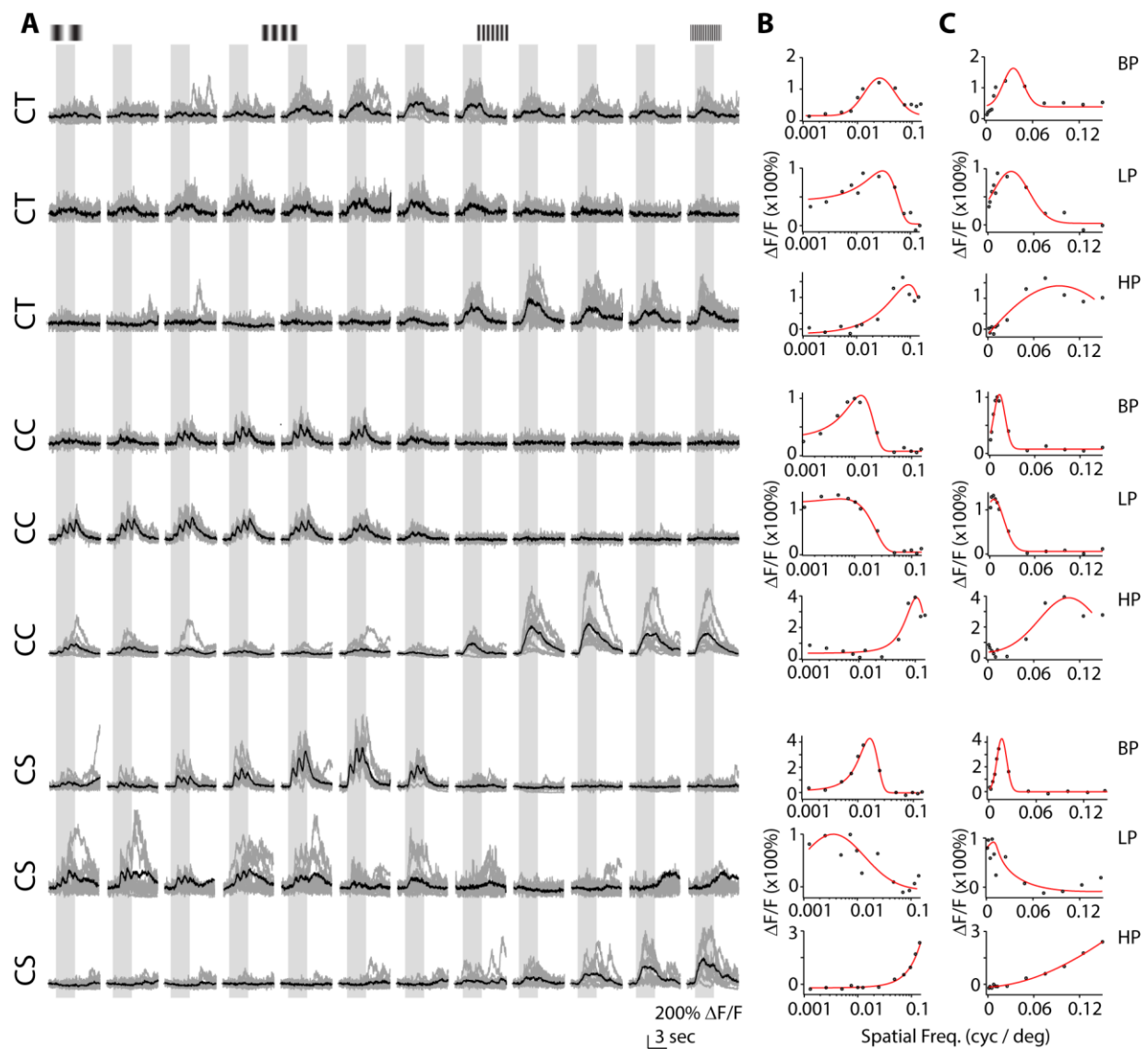
Figure S5. Example spatial frequency curves, related to Figure 3.
(A) Example raw (gray) and average (black) traces of a CT (top three), CC (middle three) and CS (bottom three) neurons at varying spatial frequencies.
(B) Gaussian curves (red) fit over spatial frequency data (black circles) from (A) on a log10 scale.
(C) Gaussian curves (red) fit over spatial frequency data (black circles) from (A) on a linear scale. Band pass (BP), high pass (HP), and low pass (LP) cells are indicated.

Figure S6. Schematic example of noise correlation analysis, related to Figure 4.
(A) Schematic representation of the pair-wise correlations calculated between neurons identified via retrograde labeling (ID-ID, left) or labeled and non-identified cells (ID-NI, right).
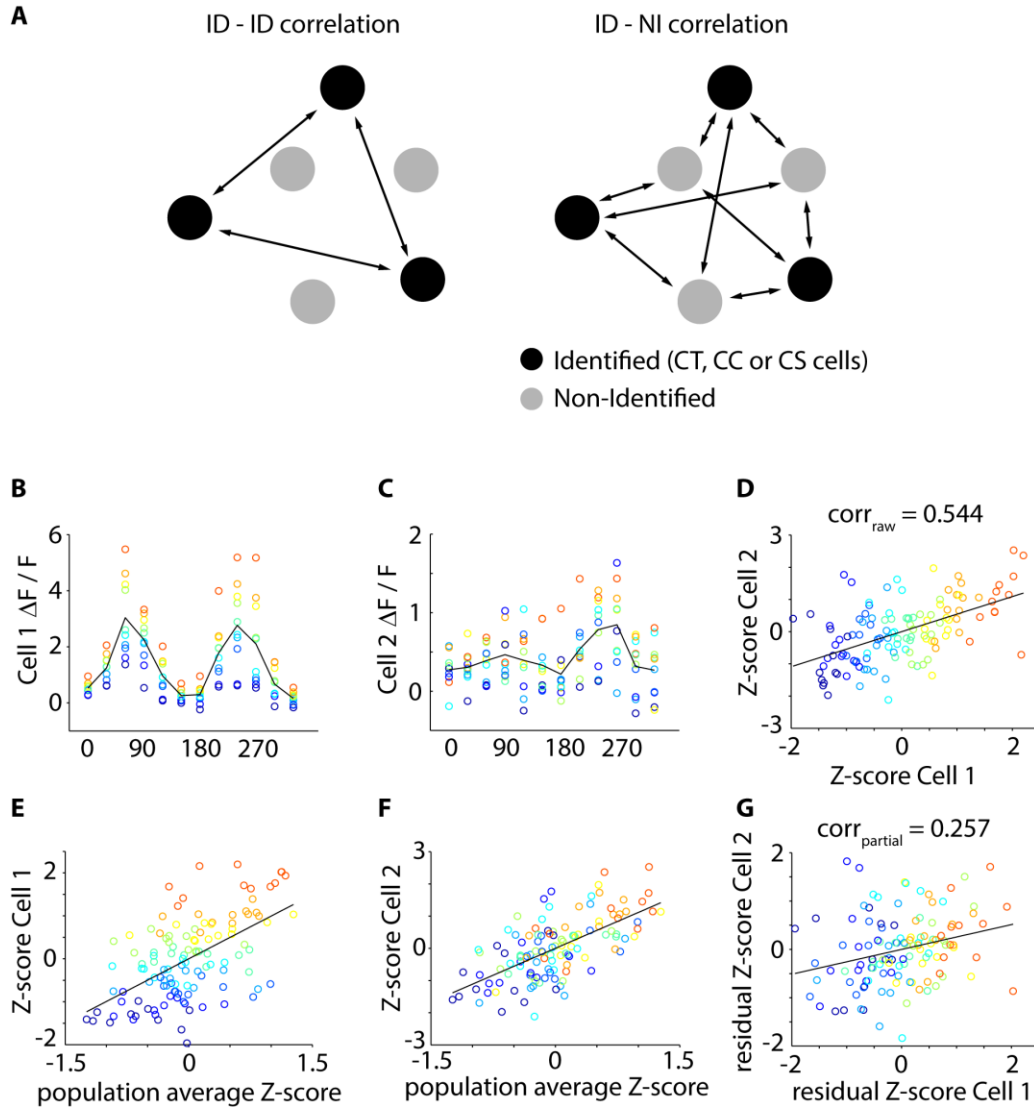(B) Orientation tuning curve (black) for Cell 1 averaged from raw data points (color coded for trial number and sorted in ascending order for response magnitude).
(C) Orientation tuning curve (black) for Cell 2 averaged from raw data points (color coded to match trial numbers in Cell 1).
(D) Individual trials were Z-scored and Cell 2 plotted against Cell 1. The slope of a linear fit to the data (black line) represents the raw correlation strength.
(E) Z-scores of Cell 1 plotted against the Z-scored average of the population activity. To account for correlations representing population activity, residual Z-score was calculated as the distance of each trial from the linear fit.
(F) Z-scores of Cell 2 plotted against the Z-scored average of the population activity. Residual Z-score was calculated as the distance of each trial from the linear fit.
(G) Residual Z-score of Cell 2 plotted against residual Z-score of Cell 1. The slope of the linear fit to the data (black line) represents the partial correlation strength between Cell 1 and Cell 2.

9

Supplementary experimental procedures

Animals

All animal handling was performed in accordance with the Yale Institutional Animal Care and Use Committee and federal guidelines.   Adolescent (6-8 week) wild type C57/bl6 mice (JAX: 000664) were obtained from Charles River Laboratory. Mice were group housed (2-5 mice) in standard cages on a 12h light-dark cycle. Both male and female mice were used for experiments.

Histology

For dual fluorescent cholera toxin B (CTB) labeling, C57/bl6 mice (p40-65) were injected with CTB-Alexa Fluor-555 and CTB-Alexa Fluor-488 at two of the three projection targets.   Injection coordinates (in mm from Bregma) were: superior colliculus AP: -2.95, ML: 0.5, DV: 2.05; contralateral medial V2 AP: -3.1, ML: 1.2, DV: 0.5-0.2; dorsal striatum AP: +0.25, ML: 1.6, DV: 1.8. After 1-2 weeks, mice were transcardially perfused with ice cold phosphate buffer (PB) followed by ice cold 4% paraformaldehyde (PFA, Electron Microscopy Sciences) in PB. After dissection, brains were post-fixed in 4% PFA overnight at 4 °C.   Sections (30 μm) containing the primary visual cortex were cut on a vibrotome (Leica) and washed in PB. Slices were mounted on microscope slides and fluorescent cell bodies visualized on an upright BX53 fluorescent microscope (Olympus). Images of the entire visual cortex (~25 slices / animal) were obtained via an automated microscope stage. Labeled cells in every section were automatically counted in ImageJ. For cell reconstructions, slices used for electrophysiology (see below) were fixed in 4% PFA for 1 hour at 4 °C and stained with 5μg/ml Streptavidin Alexa Flour 546 (Invitrogen) in phosphate buffer also containing 0.1% Triton-X100 and 1% BSA for 3 hours at room temperature. Neurons were then imaged on a BX51 upright fluorescent microscope (Olympus), and Z-projections were traced in Neuromantic (Darren Myatt, Reading, UK) software.

Acute slice experiments

Acute brain slices were prepared from the primary visual cortex. Under isoflurane anesthesia, mice were decapitated and coronal slices (300 μm) were cut in ice-cold external solution containing (in mM): 110 choline, 25 $NaHCO_3$, 1.25 NaH_2PO_4, 3 KCl, 7 $MgCl_2$, 0.5 $CaCl_2$, 10 glucose, 11.6 sodium ascorbate and 3.1 sodium pyruvate, bubbled with 95% O_2 and 5% CO_2. Slices containing V1 were then transferred to artificial cerebrospinal fluid (ACSF) containing (in mM): 126 NaCl, 26 $NaHCO_3$, 1.25 NaH_2PO_4, 3 KCl, 1 $MgCl_2$, 2 $CaCl_2$, 10 glucose, bubbled with 95% O_2 and 5% CO_2. After an incubation period of 15 min at 34 °C, the slices were maintained at 22–24 °C for at least 20 min before use. Whole-cell patch-clamp recordings were obtained from layer 5 pyramidal cells (400-500 μm from the pial surface) identified with video-infrared/differential interference contrast. CTB-Alexa Fluor-555-labeled cells were identified under fluorescent illumination using a mercury lamp and appropriate bandpass filters (Semrock) on a BX51 upright microscope (Olympus).   For current-clamp recordings, glass electrodes (1.8-3.0 MΩ) were filled with internal solution containing (in mM): 135 $KMeSO_3$, 10 HEPES, 4 $MgCl_2$, 4 Na_2ATP, 0.4 NaGTP, 10 sodium creatine phosphate and 0.2% Neurobiotin (Vector Laboratories) adjusted to pH 7.3 with KOH.   Electrophysiological recordings were made using a Multiclamp 700B amplifier (Molecular Devices), filtered at 4 kHz, and digitized at 10 kHz using ScanImage (Pologruto et al., 2003). All membrane potential values were corrected post-hoc for a liquid junction potential of 7.7 mV.

2-photon imaging was accomplished with a custom-modified Olympus BX51-WI microscope (Olympus, Japan), including components manufactured by Mike's Machine Company (Higley and Sabatini, 2010). GCaMP6s was excited using 940 nm light from a pulsed titanium-sapphire laser (Ultra2, Coherent). Emitted green photons were separated with appropriate optics (Chroma, Semrock) and collected by a photomultiplier tube (Hamamatsu). In whole cell patch clamp recordings, CTB-Alexa Fluor-

555-labeled layer 5 neurons were current clamped at -60 mV and action potentials were elicited by brief current injections (2 ms, 2 nA). The number of action potentials was varied from 1 to 10 at 20 Hz or 5 action potentials were evoked at frequencies varying from 1 to 50 Hz. Fluorescence changes were collected in a line across the soma at 500 Hz and analyzed using custom routines written in MATLAB (Mathworks) and IgorPro (Wavemetrics).

Surgery for *in vivo* imaging experiments

      To express the genetically encoded calcium indicator GCaMP6s, mice were anesthetized with 1-2% isoflurane (vol/vol) mixed with pure oxygen and a small craniotomy was made over primary visual cortex. Each mouse received two 100 nl injections of adenoassociated virus (AAV2.5-*hsynapsin1*-GCaMP6s, University of Pennsylvania Vector Core) at coordinates (in mm from Bregma): AP -3.5, ML 1.8, DV 0.45 and AP -2.8, ML 2.5, DV 0.45. Injections were made via beveled glass micropipette at a rate of ~10 nl/min. After injection, pipettes were left in the brain for ~5 minutes to prevent backflow.

      During the same procedure, to retrogradely label projection-specific subtypes of L5 PNs, 200 nl of CTB-Alexa Fluor-555 was injected into either the SC, dStr, or cV2 as described above. Imaging experiments were conducted 25-30 days after virus injection. Mice were anesthetized using a mixture of ketamine (80 mg/kg) and xylazine (5 mg/kg), and a ~2 mm diameter craniotomy was opened over V1. An imaging window consisting of a small rectangular glass piece attached to a 5mm circular cover glass using an ultraviolet-curing adhesive (Norland Products) was inserted into the craniotomy and secured to the skull with dental cement (Metabond). At the same time, a surface electrode to record the electroencephalogram (EEG) was implanted anterior to the craniotomy and referenced to a second electrode in the contralateral cerebellum. A custom titanium head post was finally secured to the skull with dental cement.

Imaging

      Imaging was performed using a resonant scanner-based two-photon microscope (MOM, Sutter Instruments) coupled to a Ti:Sapphire laser (MaiTai DeepSee, Spectra Physics) tuned to 940 nm for GCaMP6 and 1000 nm for CTB-Alexa Fluor 555. Emitted light was collected using a 25x 1.05 NA objective (Olympus). The mouse was head fixed under the microscope objective, and anesthesia was switched to 0.25 – 0.75% isoflurane for a minimum of 1 hour before imaging. Throughout the recording session, mice were kept lightly anesthetized as determined by monitoring the EEG (Fig. S1A,B). Body temperature was maintained at 37 °C using a feedback-controlled heating pad (FHC). To prevent light contamination from the display monitor, the microscope was enclosed in blackout material that extended to the headpost.

      Images were acquired using ScanImage 4.2 at ~30 Hz, 256x256 pixels (290x290 μm). Imaging of layer 5 was performed at ~450-600 μm depth relative to the brain surface. For determination of visual response properties, time-series images were collected for 15,000 frames per session. Images were continuously monitored throughout the experiments, and slow drifts of the image were manually corrected. For each mouse, 1-3 fields of view were imaged per experiment. EEG signals were recorded via an FHC amplifier. EEG data and microscope frame output was digitized (5 kHz) by a Power 1401 (CED) and recorded using Spike 2 software.

Visual stimulation

      Visual stimuli were generated using custom written software in MATLAB driving a ViSaGe MKII Stimulus generator (Cambridge Research Systems). Stimuli were presented on an LCD monitor (17 inches) at a spatial resolution of 1280x960, a real-time frame rate of 60 Hz, and a mean luminance of 45 cd/m^2 positioned at a distance of 13 cm and perpendicular to the left eye. Stimuli consisted of full-screen sinusoidal drifting gratings with a temporal frequency of 1 Hz and with varied contrast,

orientation, and spatial frequency. For all experiments, visual stimuli were 3 seconds in duration and separated by an inter-stimulus interval of 5 seconds. To determine contrast response functions, orientation was fixed at 0 degrees and spatial frequency was fixed at 0.01 cycles per degree. Stimulus contrast was varied over from 10% to 100% in 10% increments and randomly presented with 10 repeats per contrast. For orientation tuning, gratings were presented at 12 different orientations spaced by 30 degrees, randomized and presented 10 times per orientation. For spatial frequency tuning, gratings were presented at 12 different frequencies from 0.0012 to 0.15 cycles per degree, randomized and presented 10 times per spatial frequency.

Data analysis

Analysis was performed using custom-written routines in MATLAB (The Mathworks) and IgorPro (Wavemetrics). Ca^{2+} imaging data was motion corrected frame by frame, and regions of interest (ROIs) were selected as previously described (Chen et al., 2013). Fluorescence was measured by averaging all pixels in a given ROI, and contamination from the neuropil was removed as previously described. Frame timing output from the resonant scanner was used to align Ca^{2+} signals with the visual stimulus post hoc. Ca^{2+} signals in response to visual stimuli were averaged and expressed as $\Delta F/F$. The $\Delta F/F$ of each trial was calculated as (F-F0)/F0, where F0 was the fluorescence averaged over the one second prior to visual stimulus presentation and F was the fluorescence averaged across the 3 seconds of visual stimulation. A cell was classified as visually responsive if the Ca^{2+} signals during stimulus presentation were statistically different from the signals during five blank periods (p<0.05, ANOVA test) and larger than 10% $\Delta F/F$.

To calculate the modulation index (MI) for each individual cell, $\Delta F/F$ traces during the presentation of the preferred orientation at 100% contrast were first de-trended by subtracting a second order polynomial fit from the data. The resulting traces were then fit by a sine function and the peak-to-trough amplitude of the resulting curve was divided by the mean total Ca^{2+} response. Contrast response curves were fit by a hyperbolic ratio function (Contreras and Palmer 2003):

$$R(C) = \frac{Rmax * C^n}{c50^n + C^n} \qquad (1)$$

The orientation selectivity index (OSI) for visually responsive cells was calculated as $1 -$ circular variance (Ringach et al., 2002). Orientation tuning bandwidth was measured as the half width at 1/sqrt2 of a flat-top von Mises function fit to the data. Alternatively, we calculated the orientation selectivity as the depth of modulation from the preferred to orthogonal orientation: OS = ($R_{pref} - R_{ortho}$) / ($R_{pref} + R_{ortho}$) (Niell and Stryker, 2008). For spatial frequency tuning, data were fit with a Gaussian function plotted on a log10-frequency scale. Cells were classified as low pass or high pass if the low or high end of the tuning curve, respectively, failed to cross the half maximum point. For band pass cells, bandwidth was expressed as the half width at 1/sqrt2 of the maximum of the fit in cycles per degree. For all analyses that required curve fitting, cells were only included if the goodness-of-fit yielded a $R^2 > 0.4$.

To estimate local functional connectivity, we performed noise correlation analyses (Cohen and Kohn, 2011). We calculated the pair-wise correlation in trial-by-trial fluctuations in response strength either between two retrogradely identified cells or between identified and non-identified cells (Fig. S6A). Correlation coefficients were computed as follows. For each given cell and stimulus direction, we Z-scored the $\Delta F/F$ responses across trials. These Z-scored responses were concatenated across stimulus directions, as in (Ecker et al., 2010) to prevent stimulus correlations from affecting correlations in spontaneous activity. The concatenated response vector is denoted x_i for the i-th cell (Fig. S6B-D). We then removed the influence of common network fluctuations by computing partial correlation coefficients (Fig. S6E,F). Thus, for a given pair of cells i and j, we computed the sum of x_k across all k for which $k \neq i$ and $k \neq j$ as

$$s = \sum_{k \neq i,j} x_k \qquad (2)$$

The variable s represents the population activity. We then computed the partial correlation coefficient between x_i and x_j, by subtracting s (Fig. S6G). The partial correlation coefficient is simply the correlation between the residuals r_i and r_j, where the residuals r_i is computed from a linear regression of x_i onto s.

Statistical analysis

   A common problem in many experimental studies is the use of nested design, where multiple cells are measured for each animal and cannot be taken as independent measurements (Cochran, 1937; Galbraith et al., 2010). To avoid the increased false positive rate inherent in nested designs, we used semi-weighted error estimators, commonly used in random-effects meta-analysis (Chung et al., 2013; DerSimonian and Laird, 1986). Let y_i be the mean for one parameter (e.g., OSI) for the i-th animal, where x_j is the parameter value for the j-th cell and there are M cells per animal, defined as:

$$y_i = \frac{1}{M} \sum_{j=1}^{M} x_j \qquad (3)$$

   The unweighted estimator of the mean is defined as the mean over y_i, using the number of animals per condition as degrees of freedom. This analysis is suboptimal, as some animals have many cells and yield more reliable estimates, whereas other animals have few cells and yield more unreliable estimates. The weighted estimator is defined by pooling observations across N animals and using the number of cells per condition as degrees of freedom. This analysis does not properly control the false alarm rate (Aarts et al., 2014). The semi-weighted estimator, for a given experimental condition (e.g., CT cells) is defined as:

$$\mu = \frac{\sum_{i=1}^{N} w_i y_i}{\sum_{i=1}^{N} w_i} \qquad (4)$$

where weight for the i-th animal is defined as:

$$w_i = \frac{1}{\tau^2 + s_i^2} \qquad (5)$$

Here, s_i^2 is the within-animal variance across cells and τ^2 is the estimated variance across all animals of a given condition using the maximum likelihood method (Chung et al., 2013):

$$\tau^2 = \frac{\sum_{i=1}^{N} w_i \left[(y_i - \mu)^2 - s_i^2 \right]}{\sum_{i=1}^{N} w_i} \qquad (6)$$

We solved equations 5 and 6 iteratively and checked for convergence of τ^2 to <0.001. Intuitively, if there is no across-animal variance, then the contribution of each cell is weighted by the number of animals (the weighted estimator). If the across animal variance is very large (i.e., observations within an animal are maximally dependent), then each animal is given the same weight.

   We used this semi-weighted estimator to calculate the statistical significance of the difference between cell populations using a standard Student's t-test. The only exception to this was the noise correlation analysis in Figure 4, where we used the weighted estimator to reflect the pair-wise nature of the comparisons.

Supplemental references

Aarts, E., Verhage, M., Veenvliet, J.V., Dolan, C.V., and van der Sluis, S. (2014). A solution to dependency: using multilevel analysis to accommodate nested data. Nature neuroscience *17*, 491-496.

Chen, T.W., Wardill, T.J., Sun, Y., Pulver, S.R., Renninger, S.L., Baohan, A., Schreiter, E.R., Kerr, R.A., Orger, M.B., Jayaraman, V.*, et al.* (2013). Ultrasensitive fluorescent proteins for imaging neuronal activity. Nature *499*, 295-300.

Chung, Y., Rabe-Hesketh, S., and Choi, I.H. (2013). Avoiding zero between-study variance estimates in random-effects meta-analysis. Statistics in medicine *32*, 4071-4089.

Cochran, W.G. (1937). Problems Arising in the Analysis of a Series of Similar Experiments. Supplement to the Journal of the Royal Statistical Society *4*, 102-118.

Cohen, M.R., and Kohn, A. (2011). Measuring and interpreting neuronal correlations. Nature neuroscience *14*, 811-819.

DerSimonian, R., and Laird, N. (1986). Meta-analysis in clinical trials. Controlled clinical trials *7*, 177-188.

Ecker, A.S., Berens, P., Keliris, G.A., Bethge, M., Logothetis, N.K., and Tolias, A.S. (2010). Decorrelated neuronal firing in cortical microcircuits. Science *327*, 584-587.

Galbraith, S., Daniel, J.A., and Vissel, B. (2010). A study of clustered data and approaches to its analysis. The Journal of neuroscience : the official journal of the Society for Neuroscience *30*, 10601-10608.

Higley, M.J., and Sabatini, B.L. (2010). Competitive regulation of synaptic Ca2+ influx by D2 dopamine and A2A adenosine receptors. Nature neuroscience *13*, 958-966.

Niell, C.M., and Stryker, M.P. (2008). Highly selective receptive fields in mouse visual cortex. The Journal of neuroscience : the official journal of the Society for Neuroscience *28*, 7520-7536.

Pologruto, T.A., Sabatini, B.L., and Svoboda, K. (2003). ScanImage: flexible software for operating laser scanning microscopes. Biomedical engineering online *2*, 13.

Ringach, D.L., Shapley, R.M., and Hawken, M.J. (2002). Orientation selectivity in macaque V1: diversity and laminar dependence. The Journal of neuroscience : the official journal of the Society for Neuroscience *22*, 5639-5651.